ELSEVIER

Contents lists available at ScienceDirect

Acta Biomaterialia

journal homepage: www.elsevier.com/locate/actbio



Full length article

Extracellular matrix regulation of cell spheroid invasion in a 3D bioprinted solid tumor-on-a-chip



Elvan Dogan^a, Christopher A. Galifi^b, Berivan Cecen^c, Roshni Shukla^a, Teresa L. Wood^b, Amir K. Miri^{a,d,*}

- ^a Department of Biomedical Engineering, Newark College of Engineering, New Jersey Institute of Technology, Newark, NJ 07102, USA
- Department of Pharmacology, Physiology, and Neuroscience and Center for Cell Signaling, Rutgers New Jersey Medical School, Newark, NJ 07103, USA
- ^c Department of Biomedical Engineering, Rowan University, Glassboro, NJ 08028, USA
- d Department of Mechanical and Industrial Engineering, Newark College of Engineering, New Jersey Institute of Technology, Newark, NJ 07102, USA

ARTICLE INFO

Article history: Received 12 March 2024 Revised 1 July 2024 Accepted 25 July 2024 Available online 7 August 2024

Keywords:
Solid tumor spheroid
Bioprinting
Microstructure
Mechanobiology
Gelatin

ABSTRACT

Tumor organoids and tumors-on-chips can be built by placing patient-derived cells within an engineered extracellular matrix (ECM) for personalized medicine. The engineered ECM influences the tumor response, and understanding the ECM-tumor relationship accelerates translating tumors-on-chips into drug discovery and development. In this work, we tuned the physical and structural characteristics of ECM in a 3D bioprinted soft-tissue sarcoma microtissue. We formed cell spheroids at a controlled size and encapsulated them into our gelatin methacryloyl (GelMA)-based bioink to make perfusable hydrogel-based microfluidic chips. We then demonstrated the scalability and customization flexibility of our hydrogel-based chip via engineering tools. A multiscale physical and structural data analysis suggested a relationship between cell invasion response and bioink characteristics. Tumor cell invasive behavior and focal adhesion properties were observed in response to varying polymer network densities of the GelMA-based bioink. Immunostaining assays and reverse transcription-quantitative polymerase chain reaction (RT-qPCR) helped assess the bioactivity of the microtissue and measure the cell invasion. The RT-qPCR data showed higher expressions of HIF-1 α , CD44, and MMP2 genes in a lower polymer density, highlighting the correlation between bioink structural porosity, ECM stiffness, and tumor spheroid response. This work is the first step in modeling STS tumor invasiveness in hydrogel-based microfluidic chips.

Statement of significance

We optimized an engineering protocol for making tumor spheroids at a controlled size, embedding spheroids into a gelatin-based matrix, and constructing a perfusable microfluidic device. A higher tumor invasion was observed in a low-stiffness matrix than a high-stiffness matrix. The physical characterizations revealed how the stiffness is controlled by the density of polymer chain networks and porosity. The biological assays revealed how the structural properties of the gelatin matrix and hypoxia in tumor progression impact cell invasion. This work can contribute to personalized medicine by making more effective, tailored cancer models.

© 2024 Acta Materialia Inc. Published by Elsevier Ltd. All rights are reserved, including those for text and data mining, Al training, and similar technologies.

1. Introduction

The high mortality in cancer patients is primarily attributed to metastatic tumor spread, recurrence, and resistance to anti-cancer treatments. The mechanisms underlying drug-resistant tumors and

E-mail address: am3296@njit.edu (A.K. Miri).

their recurrences remain unknown [1,2]. In the case of soft-tissue sarcoma (STS), which has relatively few effective systemic therapies [3,4], and optimum disease management requires predictive cancer models using patient-derived tumor cells and carrying host genetic information. The established cancer models that utilize patient-derived samples include gold-standard xenografts, static three-dimensional (3D) spheroids, and dynamic culture models [5,6]. The well-established xenograft models are time-consuming and suffer from unrealistic genomic profiling of sample biopsies

^{*} Corresponding author at: 323 Dr. Martin Luther King Jr Blvd, Fenster Hall 624, Biomedical Engineering Department, Newark, NJ 07102-1982.

[7–9]. While static spheroids lack physiological conditions, dynamic *in vitro* models can mimic the tumor microenvironment (TME) for studying scientific questions related to tumor mechanisms and screening applications. One of our main objectives is to study solid tumor invasion under controlled conditions (i.e., regulate TME cues and monitor cell proliferation).

Microfluidics-based, micro-engineered tumors-on-chips have been recently used to mimic various tumor cell-ECM, tumorstroma, and cell-drug interactions under controlled flow conditions [10–12]. Active perfusion creates a dynamic environment to control the delivery of various components (e.g., oxygen, nutrients, etc.) to replicate the physiological conditions of solid tumors better [13]. For example, Wan et al. investigated how a constant nutrient supply impacts ovarian cancer cell spheroids in 3D culture. They used a perfusion mono and cocultured tumor spheroid bioreactor for up to 35 days to observe cancer cell growth and test drug responses. Their findings showed that, unlike static cultures that exhibit more cell stress and unpredictable reactions to treatments, the perfused cultures using microchannels and microchambers led to more realistic therapeutic responses [14]. The engineered microtissues can be bioactive matrices, such as matrigel, gelatin, collagen, and fibrinogen [5]. As an example, Refet-Mollof et al. [15] made a hypoxic jumbo spheroid-based model. The team used soft lithography to create a microfluidic chip measuring 80 mm x 82.5 mm, which holds up to 240 tumor spheroids of > 750 µm in diameter, as aggregaes of human leimyosarcoma cells. They examined the response of combined radiotherapy and the hypoxic prodrug tirapazine to giant spheroids generated using STS117 and SK-LMS-1 sarcoma cell lines. Thus, such microfluidic models allow studying TME cues in tumor mechanobiology.

A well-documented characteristic of solid tumors is increased matrix stiffness [16,17]. The matrix is dynamically regulated by cancer and stromal cells. Traditional 2D models have supported the link between matrix stiffness and tumor cell behavior, mainly reported for carcinoma and sarcoma-type cancers [18-20]. Altering the stiffness of 3D matrices can have variable effects on cancer phenotypes [21-23]. For example, Malandrino et al. assessed the role of forces that breast cancer cells (MDA-MB-231) exert on ECM. They showed that cellular forces can gather ECM fibers around the cell periphery, influenced by the dynamic tensional state of the actin cytoskeleton [21]. In addition, Liang et al. [22] showed that hepatocellular carcinoma cells formed malignant spheroids in a softer, fat-like hydrogel. Compact hepatoids with reduced malignancy were obtained in a stiffer gel. In another study, a 3D bioprinted osteosarcoma model revealed the effects of matrix stiffness on osteosarcoma cells when varying stiffnesses: 50, 80, and 130 kPa [24]. They observed increased proliferation, enhanced migration, stretched morphology, and reduced drug sensitivity in softer 3D matrices. An uptick in matrix metalloproteinase (MMP) and vascular endothelial growth factor (VEGF) secretion was reported for stiffer matrices, suggesting a survival mechanism and vascular invasion. The transcriptomic analysis pinpointed a potential impact on the integrin α 5-MAPK signaling pathway. The variety of observations suggests the uncertain effect of matrix stiffness on tumor cell behavior within the 3D ECM [21]. A recent study found an association between ECM-related genes and STS prognosis [25], in which a subgroup of dedifferentiated liposarcoma patients with poor prognosis expressed higher levels of ECMremodeling proteins.

A signaling pathway affected by TME conditions is the hypoxia-inducible factors- 1α (HIF- 1α) pathway, which is upregulated in response to hypoxia, triggering gene expression in angiogenesis, glycolysis, and invasion [26]. Hypoxia can drive cancer cell stemness, resulting in chemotherapy resistance [27] and the Warburg effect [28]. A screening tumor model should include hypoxia-related factors. In addition, the ECM properties can modulate the concentra-

tion of MMP2 and MMP9 enzymes that degrade the ECM and make space for cell invasion [29]. CD44, a surface glycoprotein implicated in cell adhesion and mobility, is mediated by cancer cells within stiff matrices [30]. It is also considered a marker for cancer stem cells [31].

There has been a trend of hydrogel-based bioinks being used in 3D bioprinted tumor models, such as Matrigel [32], gelatin [33], hyaluronic acid [34], alginate [35], polyethylene glycol [36], collagen [37], fibrin [38], agarose [39], and silk fibroin [40]. Each bioink has unique characteristics suitable for a specific tumor model, depending on the specific requirements for physical properties (e.g., stiffness and pore size) and cell-ECM interactions. Gelatin methacryloyl (GelMA), a chemically modified version of gelatin [41,42], benefits from tunable physical [43] and optical transparency [44]. GelMA has been investigated as a 3D matrix with various breast cancer cell lines for modeling drug response and invasion [45-47]. The permeability, stiffness, and degradation time of GelMA can be tailored via methacrylation degree, UV light intensity, and backbone mass concentration [48]. 3D bioprinting technology also offers a customizable platform and scalability to fabricate complex cellular arrangements under controllable conditions and high throughput manufacturing [11]. GelMA has shown cell encapsulation capacity, tunable mechanical properties, costeffectiveness, and ability to maintain the cell phenotype [49,50]. While GelMA has been used for other solid tumor models, such as breast [51] and prostate [52], it has not been used to model STS.

In this work, we engineered a GelMA-based STS microtissue via 3D bioprinting and tunability of GelMA bioink. As shown in Fig. 1, our bioprinting approach can be applied to similar photocrosslinkable hydrogel bioinks in the field. We designed and fabricated a microtissue via cell-laden hydrogel bioprinting to regulate the porosity of the ECM. We constructed a biomaterial-based tumor model for replicating STS spheroids, ECM, and active perfusion interactions. We characterized the behavior of tumor cells using gene expression measurements, immunostaining assays, and cell tracking. As a first step for modeling STS invasion, we demonstrated the formation of rounded spheroids with high reproducibility and compactness, which is essential for creating a realistic TME. We observed that the bioink composition significantly influences cell invasive behavior and focal adhesion formation of the tumor spheroids. GelMA matrices with a reduced hydrogel network promoted higher spheroid invasiveness and proliferation. RTqPCR data revealed that lower hydrogel network density correlates with increased expression of genes associated with invasiveness and hypoxia, providing valuable insights for optimizing 3D bioprinted models for cancer research.

2. Material and methods

2.1. Cell preparation

A human fibrosarcoma cell line (HT1080; ATCC; Manassas, VA) was cultured in Dulbecco's Modified Eagle Medium mixed with 10 % v/v fetal bovine serum (FBS) and 1 % v/v Pen/Strep (DMEM, VWR, Radnor, PA, USA), following standard practices. All chemicals, mediums, and substrates were mainly purchased from VWR (Radnor, PA, USA), otherwise mentioned.

2.2. Cells spheroid protocol

Monoculture spheroids were prepared with an initial seeding density of 1 \times 10⁴ cells/well in 200 μL cell suspension seeded to a non-adherent round-bottom 96-well plate (Corning, NY, USA). Three different cell passages of HT1080 were used to ensure variability. The ultra-low attachment (ULA) plates were centrifuged at 2500 rpm /850 xg for 5 min in a plate centrifuge device (VWR,

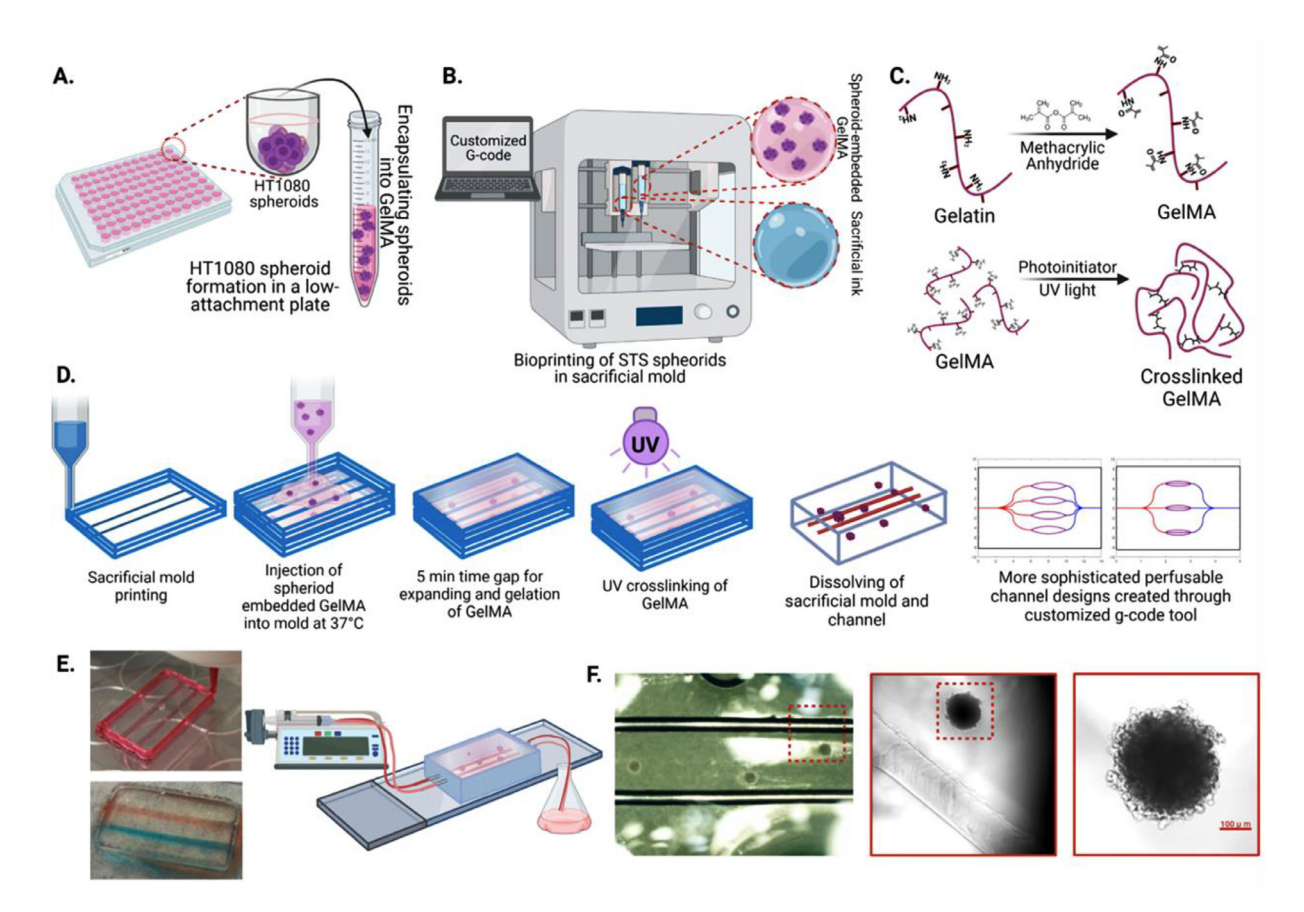


Fig. 1. The fabrication process: **A.** Soft tissue sarcoma (STS) spheroid formation and encapsulation in low-attachment well-plates; **B.** Multi-material bioprinter used to extrude the 3D hydrogel construct; **C.** Chemistry of gelatin methacryloyl (GelMA) functionalized with methacrylic anhydride; **D.** Bioprinting strategy for our 3D hydrogel microfluidic chip using spheroid embedded GelMA and sacrificial ink showing the details and parts and more sophisticated perfusable channel patterns created through our customized g-code tool; **E.** Two bioprinted chips and the experimental setup to run fluid over time; **F.** Bioprinted spheroid-laden hydrogel chip and spheroid location at Day 0.

Radnor, PA, USA) to form spheroids through centrifugal force. At Day 3, we started quantifying spheroids' diameters and roundness through ImageJ software. Roundness is based on the ratio between the inscribed and the circumscribed circles. We imaged 28 samples, selected arbitrarily from three biological replicates in a 96-well plate, and evaluated the frequency of roundness to ensure the efficiency of the protocol. After quantification, HT1080 spheroids were encapsulated into different GelMA solutions and used for the next step.

2.3. Bioink preparation

GelMA was synthesized according to an established protocol [53]. In a 100 mL glass flask of Dulbecco's phosphate-buffered saline (DPBS) (Sigma-Aldrich, St. Louis, MO, USA) and 10% w/v porcine skin gelatin (CAS Number 9000-70-8; Sigma-Aldrich, St. Louis, MO, USA) were mixed. The flask was covered to prevent evaporation and was stirred using a magnetic stir bar on a hot plate at 60 °C until fully dissolved (around an hour). After the gelatin dissolved in the DPBS, 3 ml methacrylic anhydride (CAS:760-93-0, Sigma-Aldrich, St. Louis, MO, USA) was slowly pipetted into the solution. The temperature was turned down to 50 °C, and the solution stirred and reacted for an hour. Pre-warmed DPBS was 5x the volume of the initial solution and was added to the solution after an hour to stop the reaction. Dialysis tubing (12-14 kDa molecular weight cut-off) was used to dialyze GelMA and wash off excess methacrylic anhydride for a week, and the solutions were transferred into centrifuge tubes and stored at -80 °C. After freeze-drying, GelMA solution (5, 7, and 10% w/v) was prepared with DPBS and pre-warmed at 60 °C with constant stirring. Once fully dissolved, a final concentration of 0.5% w/v 2-Hydroxy-1-(4-(hydroxyethyl) phenyl)–2-methyl-1-propanone (Irgacure 2959, CIBA Chemicals) was used as the photoinitiator (PI) of the crosslinking process. We optimized our PI concentration based on the viability test and compressive modulus with varying PI concentrations (0.1–1 % w/v) (**Fig. S2**). GelMA solution was mixed with spheroids randomly selected from three biological replicates at the desired concentration (i.e., 50 spheroids/ml) to form our bioink. This mixture was then gently agitated to ensure even dispersion of the spheroids throughout the bioink. The visual observation through a light microscope was used to check spheroid dispersion in the bioink.

2.4. Bioprinting process

Our bioprinted chip is designed and G-coded to achieve a thickness of approximately 1.5 mm, with two parallel channels that are each approximately 500 μ m in diameter, printed as a single extruded PF-127 filament. Spheroids are arbitrarily distributed throughout the chip. We used two different bioinks via direct ink writing multimaterial BIOMAKER Bioprinter having two nozzle capacities (SunP Biotech, Cherry Hill, NJ). We optimized the input nozzle sweeping speed (~ 4.7 mm/s) and the extrusion rate (~ 270 mm/min) based on resolution trials using Pluronic F-127 (Sigma Aldrich, St. Louis, MO, USA) with a 25 G needle (**Fig. S6**) to print sacrificial structure of the chip.

The bioprinted chips were then crosslinked for 3 min or 6 min (10 mW/cm²) using a UV-crosslinker (VWR, Radnor, PA, USA;

365 nm). We also created a perfusable channel and conducted a perfusion test to show the shape fidelity of the channel (**Fig. S6**). The perfusion test was then conducted with an aqueous solution of $\sim\!10~\mu m$ polystyrene microparticles (Sigma-Aldrich, St. Louis, MO) at a 30 $\mu l/min$ flow rate with an infusion pump (WRI, Sarasota, FL). Detailed information about our customized g-code generator tool is in a supplementary file (**Fig. S4–6**). Then, we washed the Pluronic F127 channel to obtain a perfusable channel [54]. The channel was used to feed the chip via a culture medium.

2.5. Mechanical characterization

Standard compression testing was performed to determine the material's stiffness under physical load. We followed a standard protocol [55] and fabricated disk-shape samples of 10 mm in diameter and 5 mm in height. We placed samples between the metal flat plates of the universal testing machine (Instron, MA, USA), and the tests were performed using the strain rate of 1 mm/min. Young's modulus was calculated as the slope of the stress-strain curve from up to 10 % strain.

2.6. Biodegradation testing

GelMA hydrogels with 10 mm in diameter and 5 mm in height were tested for enzymatic degradation. They were placed in DPBS for 3 h at 50 °C to reach the equilibrium swelling and were then transferred (n=4) into solutions with 0.55 $\mu g \, \text{mL}^{-1}$ collagenase [56]. Their enzyme degradations were conducted at 37 °C, and the images were taken during the degradation. The samples were weighed, and the mass loss percentage was calculated as [57] [(Wt – Wo) / Wo] ×100, where Wt is the weight of each GelMA hydrogel at time t, Wo is the initial weight of each GelMA hydrogel while in the equilibrium swelling.

2.7. Swelling testing

To measure the effect of GelMA concentration on hydrogel swelling, we prepared samples to form 5 mm thick x 10 mm diameter disks using a mold. We crosslinked for 3 min (10 mW/cm²) and freeze-dried before recording the dry weight (W_d). Next, the hydrogels were re-hydrated in DPBS buffer overnight at 37 °C, and the swollen weights (W_s) were recorded. The percentage degree of swelling (%) was measured as [57] [(W_s - W_d)/ W_d] × 100, where W_s is the weight of swollen GelMA hydrogel at measuring time, W_d is the dry weight of hydrogel samples.

2.8. Scanning electron microscopy imaging

For performing scanning electron microscopy (SEM), the hydrogel precursor solutions were made in a custom-built polydimethylsiloxane (PDMS) mold to prepare disk-shaped samples of 10 mm in diameter and 5 mm in height. Samples were placed in an incubator in DPBS for 24 h at 37 °C, and swollen hydrogels were frozen and subsequently lyophilized. The lyophilized samples were cut, and their cross-sections were coated with platinum using a turbo sputter coater (EMITECH, K575X), before SEM imaging (JSM-7900F Schottky Field Emission Scanning Electron Microscope). The quantifications of the porosity and aspect ratio were analyzed by ImageJ software.

2.9. Cell assays and invasion area quantification

To observe the invasive behavior of cells in spheroid-laden chips, we captured images using the Nikon Eclipse Ti-2 fluorescent

microscope (Nikon, Melville, NY, USA) through bright-field imaging for five days post-encapsulation. We developed a customized smallest enclosing circle algorithm tool in MATLAB for image processing and quantifying the invasion area (more details in **Fig. S7**). The viability of encapsulated cells and spheroids in GelMA was assessed using one Live/Dead assay (PromoCell GmbH, Heidelberg, Germany). The chips were washed with PBS (Sigma-Aldrich, USA), incubated for 40 min with calcein-AM (1 mM; live cells in green) and ethidium homodimer 1 (6 mM; dead cells in red), and then re-washed. Encapsulated cells (**Fig. S2**) and spheroids (**Fig. S8**) in GelMA were then imaged in the microscope through FITC and TRITC filters.

2.10. Immunostaining

Spheroids were analyzed by Actin Cytoskeleton / Focal Adhesion Staining Kit (FAK100, Millipore Sigma, USA), consisting of TRITC-conjugated phalloidin, anti-Vinculin and DAPI for the immunofluorescent staining of actin and vinculin filaments in the cytoskeleton as well as the nucleus of the cells. Cells were fixed with Image-iTTM fixative solution (4 % paraformaldehyde, Thermo Fisher) for 15 min, washed with DPBS (Thermo Fisher), permeabilized with 0.2 % Triton X-100 (Sigma-Aldrich) in DPBS for 30 min, blocked with 1 % bovine serum albumin (BSA) blocking buffer (Alfa Aesar, Haverhill, MA) for 1 hour, and then incubated with TRITC-conjugated phalloidin (1 μ g/mL, Millipore Sigma, FAK100) in 1 % BSA for 2 h. Samples were washed three times in DPBS and mounted on slides with DAPI for nuclear counterstain.

Spheroids were also stained with anti-Ki-67. The primary antibody for Ki-67 diluted in BSA (1:100; purified mouse anti-Ki-67, BD Pharmingen) was subsequently incubated overnight at 4 °C. Samples were washed with PBS and incubated with the secondary antibody IgG (H+L) (1:500; anti-mouse, Invitrogen) overnight at 4 °C. The samples were washed with PBS, incubated with DAPI (1:500 in PBS; Millipore Sigma) for 20 min at room temperature, and washed twice with PBS. Images were captured with the fluorescent microscope.

2.11. Gene expressions analysis

First, we used a collagenase solution to collect STS spheroids for real-time polymerase chain reaction (RT-qPCR) analysis. We used 1 mg/ml collagenase (IA, 125 CDU/mg, Sigma-Aldrich, St. Louis, MO, USA) and degraded cell-laden GelMA samples for 6 h. Samples were collected into small centrifuge tubes and centrifuged using accuSpin Micro 17 (Fisher Scientific, Pittsburgh, PA, USA) at 10,000×1 g, for 10 min, then the supernatant was removed, and samples were resuspended in RLT buffer from the RNeasy Mini Kit from Qiagen. RNA was extracted using the RNeasy Mini Kit per the manufacturer's instructions. RNA concentrations were measured using the NanoDrop ND-1000 (Thermo Scientific) and normalized to 500 ng of RNA for cDNA synthesis. cDNA was synthesized using the iScript cDNA Synthesis Kit by BioRad per the manufacturer's instructions. cDNA samples were diluted 1:10 in RNase-free water and plated in technical triplicate, and RT-qPCR was performed using the BioRad CFX96 model and RT² SYBR Green ROX qPCR Mastermix by Qiagen. Primers were purchased from IDT, and sequence or catalog information is presented in Supplementary Materials (see **Table S1**). HIF- 1α , CD44, MMP2, and MMP9 expression levels were normalized to β -actin using the ggene96 Excel macro (BioTechniques Software Library) [58]. Data was compiled in Prism9 GraphPad, and significance was determined between spheroid groups using a one-way ANOVA and subsequent Tukey's multiple comparisons test in GraphPad with alpha set at

2.12. Statistical analysis

Statistical analysis was performed using the GraphPad Prism9 statistical tool. A one-way analysis of variance (one-way ANOVA) test was used for data analysis. A value of p < 0.05 was considered to be statistically significant. Relative fluorescent intensities in the images were quantified using ImageJ.

3. Results and discussions

3.1. Spheroid characterization

We characterized the spheroid morphology via the colony shape's regularity, known as the roundness [59,60]. Spheroids' circular morphology and roundness indicate the degree of cell-cell adhesion, uniformity of cell distribution, and overall structral integrity. Our results showed the creation of rounded spheroids with a slightly left-skewed normal distribution of roundedness within a ULA plate (Fig. 1A and Fig. S1). We calculated the projected area and circularity to measure the spheroid size according to the cross-sectional area of cell spheroids using ImageJ at Day 3 and on a ULA plate. The average cross-sectional diameter is 428 \pm 18 μ m, and circularity degrees obtained from the spheroids indicated circular morphology with values ranging 0.83 - 0.98 (n=28). A high circularity is important for the scalability and repeatability of the bioink for the high-throughput manufacturing of our model.

We then studied the effect of the bioink composition and fabrication process on the spheroids and the geometrical features. We observed ECM secretions throughout the spheroid culture in the ULA, which ensure compactness and an increased roundness of the spheroids consistent with the literature [59,61]. The compactness will create essential TME cues, such as hypoxia, leading to well-organized tumor growth and subsequent ECM remodeling via the regulation of MMPs and other cellular factors.

3.2. Biophysical characterization of bioinks

We evaluated the influences of the bioink mass concentrations on the physical/mechanical properties and biodegradability of the bioprinted structures (Fig. 2) [43,62,63]. Preliminary studies showed that a concentration between 5 and 10% w/v offers ideal cell viability and promotes proliferation [47,64]. At three concentrations of 5, 7, and 10% w/v, stress versus strain curves (Fig. 2Ai) and average compressive modulus (Fig. 2Aii), swelling, and degradation properties (Fig. 2Bi-iii) were obtained for this study. Fig. 2Bii shows that 5% w/v GelMA (or 5 % GelMA) swelled more compared to 7 % and 10 % GelMA, relative to its initial weight. The 10 % GelMA case degrades the slowest due to its higher network density, which arises from more crosslinked side chains, lowering the collagenase degradation rate (Fig. 2Biii). The elastic modulus represents the physical properties of the bioink at the macroscale, which is controlled by the gelatin macromere

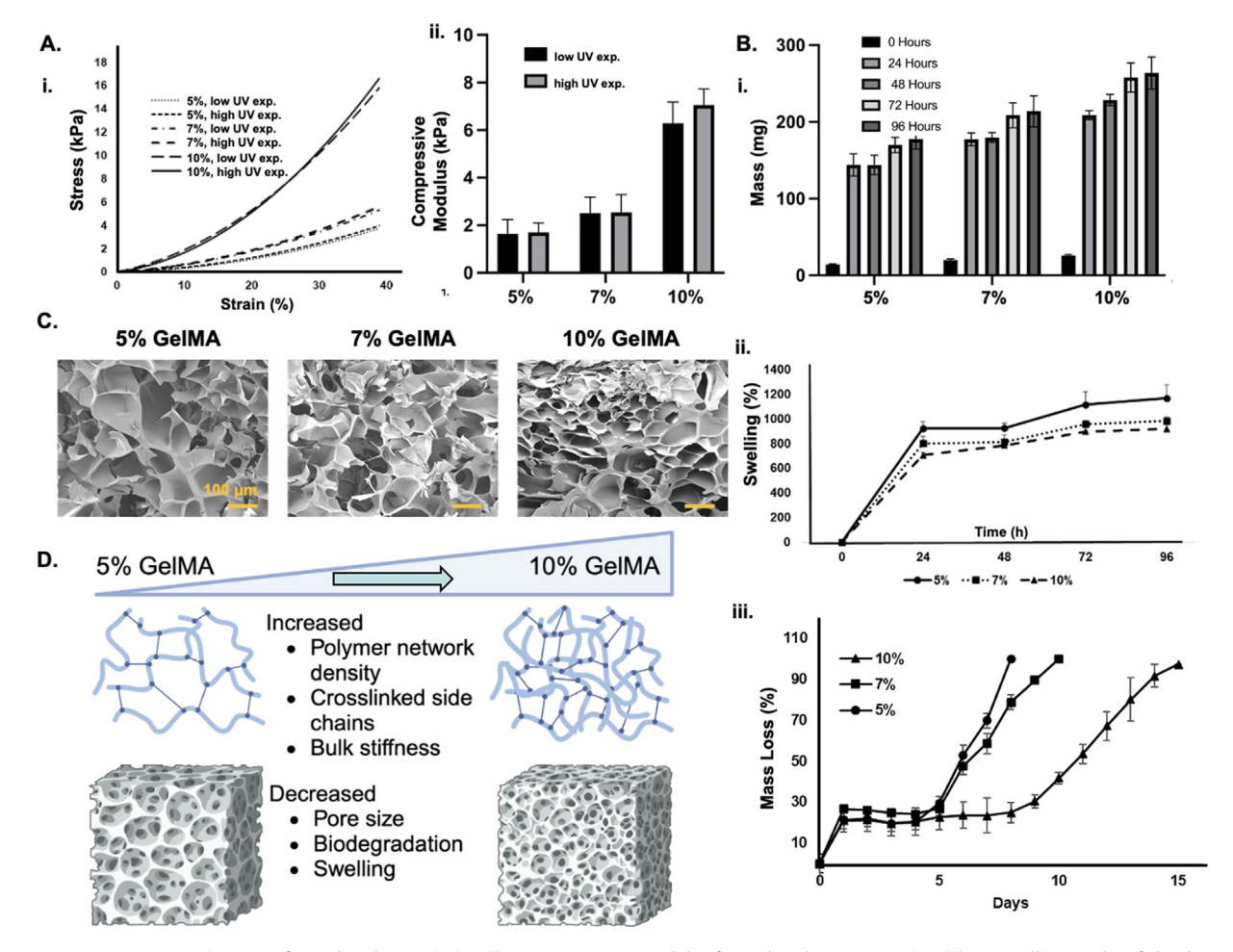


Fig. 2. A. Average stress vs. strain curves for each GelMA variation (i), average Young's modulus for each GelMA permutation (ii); **B.** Swelling results of the three different concentrations (5, 7, and 10% w/v) showing the time history (i), and percentages (ii), along with biodegradation results (iii); **C.** Porosity imaging for the three different concentrations (5, 7, and 10% w/v) through SEM (scale bar is 100 μ m); **D.** Comparative illustration demonstrating the impact of increased GelMA concentration on the biophysical properties of crosslinked GelMA. The data sets are presented as mean \pm s.d., n=4.

density and configurations at the microscale. The results belong to the small deformation and the linear response of the bioink and indicate bioink tunability.

The bulk stiffness of STS has been reported to be around 2.4 ± 1.5 kPa (range: 0.89 - 6.3 kPa) [65]. We can tune the bioink to adjust the desired stiffness for STS or other solid tumors. Higher methacrylation degrees for crosslinking the molecules and macromeres are anticipated to yield higher densities of crosslinking sites that affect the bulk elasticity [53]. Miri et al. [48] showed that from low to high methacrylation degrees, the elastic modulus increased from \sim 1 kPa to \sim 6 kPa for 10 % GelMA hydrogel at UV exposure of 30 s. Longer UV exposures of 60 s and 120 s ($\sim 100 \text{ mW/cm}^2$) further enhanced the elasticity of 10 % GelMA hydrogel up to \sim 11 kPa and \sim 14 kPa, respectively. They used indentation testing, which targets localized bioink properties at the mesoscale (i.e., between micro- and macro-scale). Increasing UV exposure time led to a higher elastic modulus, demonstrating results similar to the literature [66] but at a higher rate than our compression testing results. The differences between our minimum and maximum UV exposure groups are insignificant in this study (p > 0.05). This difference could result from a low exposure time, which provides the required energy to saturate side chain reactions during covalent bond formation. Further crosslinking did not significantly alter the bioink properties.

We compared the responses of GelMA samples with dispersed cells and spheroids up to Day 14. Acellular samples demonstrated slight mass loss where the uncrosslinked parts were dissolved. The degradation mode for dispersed cells and spheroids has different impacts on the biophysical properties of the bioink. The presence of dispersed cells may impair crosslinking [53], and the compactness of spheroids has less effect on the crosslinking, as highlighted in Fig. S10. The dispersion of cells can hamper light scattering, which may reduce the UV energy penetration; hence, 5 % GelMA hydrogels could not be effectively crosslinked and were highly deformed. On the other hand, spheroid-laden samples remained intact up to Day 14. The tumor spheroids possess different properties, such as pre-formed intercellular junctions and presynthesized native ECM [67]. We observed a significant increase in hydrogel stiffness over time in spheroid-laden samples, especially at a concentration of 10% w/v. It can be speculated that lysyl oxidase could potentially cause crosslinking in the lysine groups of the GelMA backbone [68]. This effect can be fully characterized in future work.

3.3. Role of bioink in cell invasion

Fig. 3A-C show that hydrogel network density and porosity regulated cell invasiveness. For each chip, we analyzed three randomly selected spheroids. Our SEM data (Fig. 2A) indicated a smaller pore size in 10 % GelMA versus 5 % GelMA. The average cross-sectional invasion radius of the spheroids was 214 \pm 9 μm at Day 0 (Fig. S1). At Day 5, the average calculated invasion radius was 1690 \pm 40 μm for 5 % GelMA chips and expanded \sim 300 $\mu m/day$ during the five-day observation period. The average invasion radius for spheroids embedded in 7 % GelMA was 1480 \pm 170 μm with a \sim 250 $\mu m/day$ expansion rate. The sizes of spheroids embedded in 10% w/v (237 \pm 10 μm) were unexpanded. Fig. S9 demonstrates the rapid dissociation of three biological replicates of spheroids cultured in regular culture plates. The spheroids completely dissociated and attached to the culture plate within three days.

Our findings suggest that cells exhibited more invasive behavior in a less stiff matrix. In a degradation-dependent invasion mode, rapid matrix degradation can occur in less-stiff GelMA structures [69] (Fig. 2D). Several reasons can contribute to this phenomenon. First, in softer hydrogels, cells encounter lower mechanical resistance, which eases their movement and penetration through the

matrix [70]. Cellular mechanotransduction can allow cells in a 5 % GelMA matrix to activate signaling pathways that promote cellular motility and invasiveness [71]. The capacity to remodel and degrade softer hydrogels is a key factor in migration, enabling them to create pathways for movement [72]. The improved diffusion of nutrients and oxygen in softer hydrogels creates a more conducive environment for cell growth [73].

The tumor spheroid culture demonstrated homogeneous size, growth, and high reproducibility (Fig. 3A-C). After seeding spheroids, large spheroids exhibited a heterogeneous architecture with a peripheral proliferating region as they expanded. This observation was consistent with published data showing that larger spheroids (radius > 300 μ m) developed central hypoxic cores [74]. Given the average radius of the spheroids (430 \pm 18 μ m at Day 1), we can speculate that the limited diffusion of nutrients and oxygen to cells localized in the central region inhibited their proliferative activity. It is unclear why spheroids embedded in the less stiff 5 % GelMA chip express higher levels of HIF-1 α . One explanation is that these cells are more proliferative (as indicated by our Ki-67 stain; Fig. 4D), consume more oxygen, and promote a hypoxic environment. In this work, we cannot exclude the possibility that either the matrix concentration or some other aspects of the STS phenotype contribute to more severe hypoxia in the lowest concentration (i.e., 5% w/v).

At Day 5, the cells formed viable 3D spheroids, as shown by phalloidin (red), vinculin (green), and DAPI (blue) stainings in Fig. 4. Cell growth in the microfluidic chip resulted in expansion, as confirmed with reconstructed images using fluorescence microscopy (Fig. 4). We observed that actin filaments and vinculin formation are more dense in 5 % and 7 % GelMA compared to 10 % GelMA. Previous studies suggest that ECM crosslinking and polymer density affect focal adhesion assembly, thus promoting malignant transformation [75,76]. For example, Lam et al. report that the increased stiffness of hydrogels in a 3D culture platform significantly slowed the invasion of tumor cells from 3D spheroids [77]. This result supports our model in which spheroids in a less dense (i.e., higher porous) matrix tend to invade faster. Accumulation of F-actin was primarily observed at the rim of tumor spheroids grown in hydrogels. The increase in F-actin might be associated with its reported role in protecting tissues and cells against mechanical stress [75,76]. Previously, it has been reported that hypoxic conditions can increase F-actin formation [78]. However, the exact mechanism driving this trend is unknown. One primary driver of actin polymerization is integrin binding to the ECM substrate, which regulates actin dynamics through Rho GT-Pases and downstream effectors [79]. This might suggest the enhanced F-actin signal in the 5 % GelMA case. A less stiff matrix may promote growth factors to induce actin polymerization via receptor and downstream Rac and Cdc42 activation [80]. A less dense hydrogel network could promote stem-like transformation (an increased CD44 expression level), which may explain the higher level of invasiveness in a less stiff (i.e., higher porosity) matrix than in a higher stiffness (i.e., lower porosity) matrix (see Fig. 3).

3.4. Tumor cell proliferative activity

We encapsulated STS cells within a GelMA hydrogel chip featuring active perfusion up to Day 5. Ki-67 protein is present in the cell nuclei during active phases of the cell cycle and absent in resting (non-dividing) cells. The Ki-67 expression is often correlated with the aggressiveness of the cancer, significantly influenced by the hydrogel network density. In the cases of 5 and 7 % GelMA, which represent more porous ECM, there was an accumulation of Ki-67 positive cells that increased by the reduction of the bioink concentration, as shown in Fig. 4D. The Ki-67 accumulation at the periphery of the invaded cells suggests higher proliferative

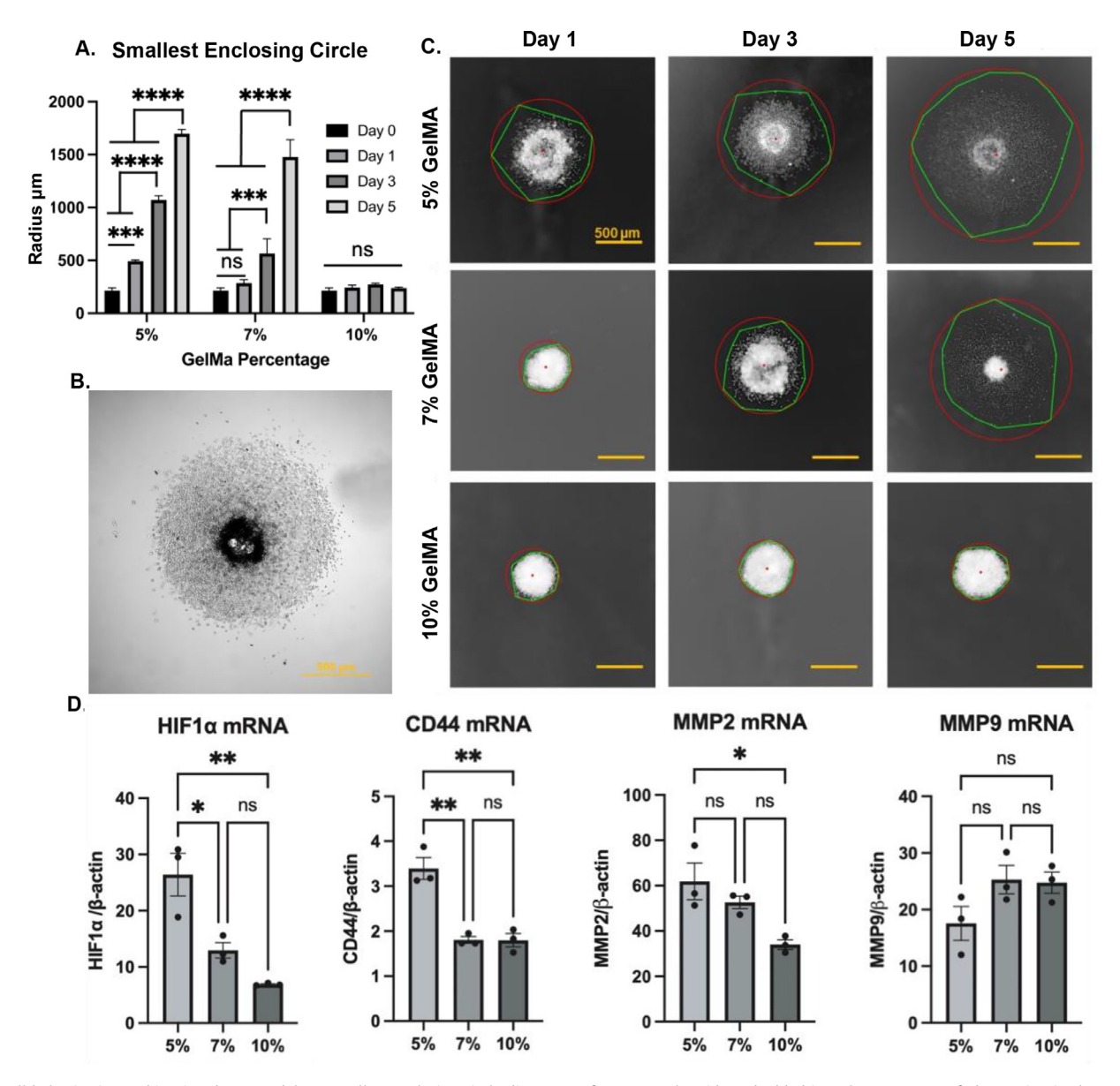


Fig. 3. Cell behavior in our bioprinted STS model: **A.** Smallest enclosing circle diameters of HT1080 spheroids embedded in GelMA at Day 5 of observation in three different GelMA concentrations; **B.** The bright field image of cell invasion behavior over time in 5 % GelMA at Day 5 for an example ($\sim 400 \ \mu m$ at Day 1); **C.** Processed images in MATLAB using convex hull and smallest enclosing circle algorithms of spheroids; **D.** HIF-1α, CD44, MMP2, and MMP9 mRNA expression values normalized to β-actin expression (the data sets are presented as mean \pm s.e., n=3).

rates and increased cell motility (Fig. 4B; Ki-67 expression was absent in 10 % GelMA). A significant increase in actin polymerization (see Fig. 4C) supports an increase in cell motility that correlates with decreasing GelMA concentration. Considering the increase in the invasion area that correlates with decreasing matrix density in Fig. 3A-C, the reduced matrix stiffness can promote both the proliferation and migration of STS cells.

The expression of vinculin in spheroids embedded in 5, 7, or 10 % GelMA was unchanged across groups (Fig. 4A-C), suggesting a similar capacity to bind matrix protein in STS cells regardless of matrix density. Our fluorescence data suggests that the invasive phenotype is attributable to increased cell motility via actin dynamics, and our qPCR data suggests that ECM remodeling through MMP function may also be involved.

MMPs related to ECM remodeling are related to cell motility [81,82]. The gelatinases, MMP2 and MMP9, degrade type IV collagen, a major component of the basement membrane [83]. Of particular interest is MMP2, as increased activity of this enzyme

correlates with poor soft tissue sarcoma prognosis [84]. As GelMA is composed of a gelatin matrix, MMP2 and MMP9 are important markers of cancer aggressiveness. A prior study analyzing mRNA expression of MMP2 and MMP9 in human patient cases of malignant fibrous histiocytoma (MFH) found that MMP2 expression was higher in metastatic versus nonmetastatic cases [85]. This is consistent with our RT-qPCR data, which show a statistically significant increase in MMP2 expression from spheroids embedded in 5 % versus 10 % GelMA. Spheroids embedded in 5 % GelMA exhibit enhanced invasiveness, suggesting that MMP2 expression correlates with an aggressive STS phenotype. This study found that MMP9 expression was lower in the metastatic cases of MFH. The invasive spheroids embedded in 5 % GelMA exhibited a trending nonsignificant decrease in expression of MMP9 compared to spheroids embedded in 7 % GelMA (p = 0.1499) and 10 % GelMA (p = 0.1816). Our results indicate that MMP2 gene expression is downregulated with the increased mass concentration, while MMP9 expression levels increase non-significantly. Decreased CD44 and HIF-1 α

E. Dogan, C.A. Galifi, B. Cecen et al.

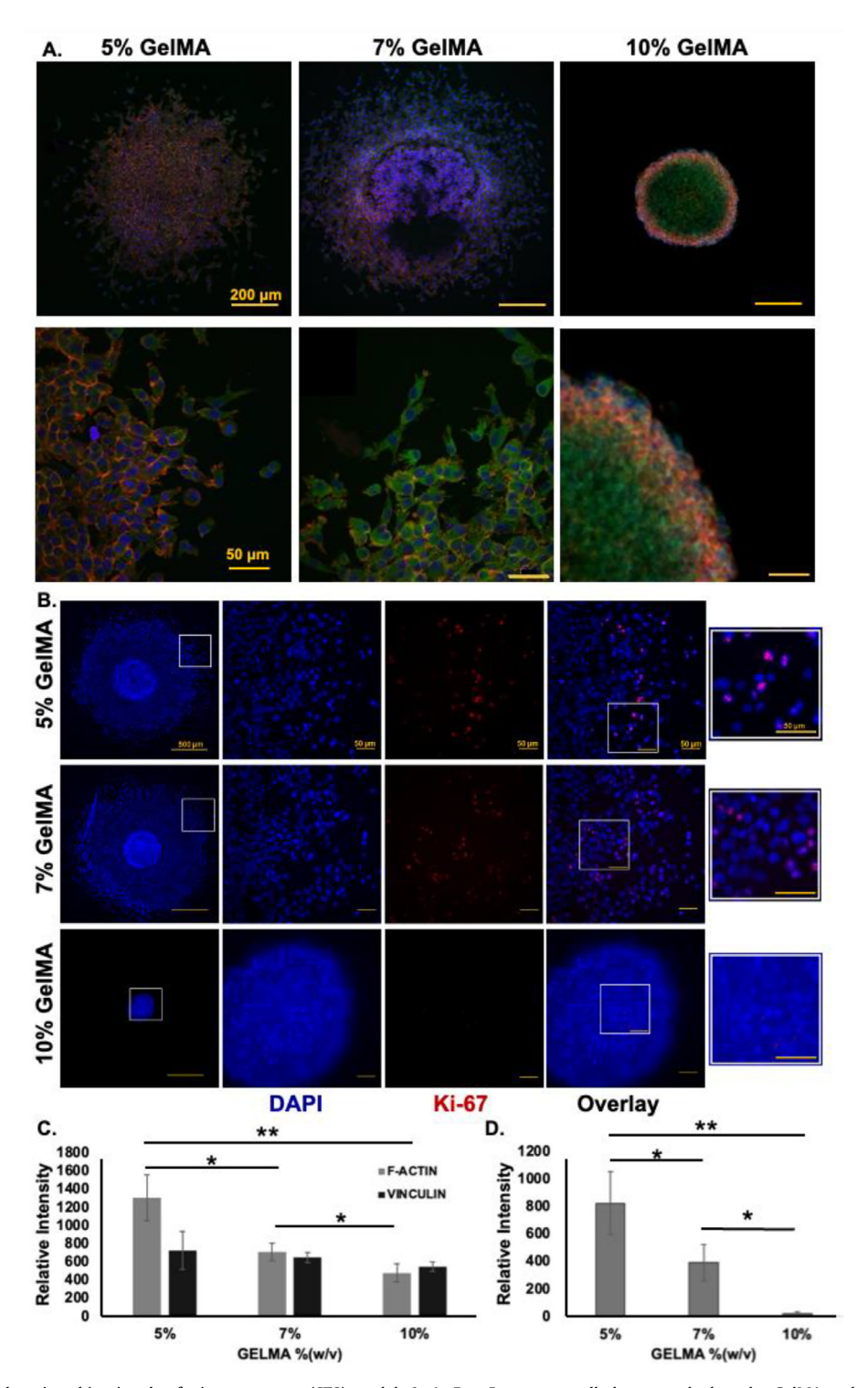


Fig. 4. Selected cell biomarkers in a bioprinted soft tissue sarcoma (STS) model. **A.** At Day 5, sarcoma cells have attached to the GelMA and migrated away from the 3D spheroids. This migration highlights certain cell components: Phalloidin is stained in red, and vinculin is stained green. DAPI is stained in blue. The scale bar is 50 μ m; **B.** Images focus on tumor cell proliferation within the GelMA environment. Ki-67 is stained red, and the cell nuclei are stained with DAPI in blue. The accumulations of proliferative cells at the periphery of the migrated area in the 5 % and 7 % GelMA concentrations are shown; **C.** Relative intensity plot of focal adhesion markers; **D.** Relative intensity plot of Ki-67 staining.

expression levels showed a parallel trend with MMP2 expression that may indicate increased aggressiveness of STS in a more porous hydrogel network (Fig. 3D). Our results also support the findings of Wang et al. that showed the positive correlation between HIF-1 α and MMP2 expression in hepatocellular carcinoma emphasizing the role of MMP2 in tumor cell invasion, and metastasis [86].

4. Concluding remarks

We engineered a first-step STS microtissue for studying solid tumor invasion and showed the reproducibility of our model through various characterizations. The hydrogel-based spheroidon-a-chip was subjected to a dynamic perfusion condition, as suggested in the literature [14,87]. The tumor cells tend to invade a compact and homogenous trend in reduced ECM network density. In contrast, an ECM network density above a threshold can prevent the invasive potential of tumor cells. The chemistry, stiffness, and porosity of synthetic or natural polymer-based scaffolds influence cellular invasion. This work focused on tunable ECM properties while simplifying factors such as cell composition. Though some recent reports recommend cell spheroid models for studying metastasis and epithelial-to-mesenchymal transition, their potential as a platform for cellular invasion studies has not been detailed. Prior studies showed that ECM properties affect focal adhesion assembly and thus promote malignant transformation [88]. Altered ECM can induce hypoxia in cancer cells [16] and regulate cancer cell invasion [89-91]. We focused on the effect of hydrogel network density, which mimics ECM properties, on MMP expression and STS invasion [92].

Most in vitro experiments use cultured cells in 2D on Poly-d-Lysine coated surfaces, Matrigel, and ECM-derived protein suspensions. Spheroid models are based on scaffold-free cell collections or cell-laden hydrogels [93]. Scaffold-free spheroids lack tumorstromal ECM interactions compared to dispersed cell-laden hydrogel models. In addition, the dispersed cell-laden hydrogel models cannot replicate the hypoxic conditions [94]. We show that manipulating GelMA concentration can stimulate variable effects on hypoxia and MMP expression. The study of hypoxic conditions and MMP function is integral to understanding metastasis. The microchannel helps deliver nutrients to tumor cells, which can be vascularized to study the intravasation of cancer cells into the circulation. The next step may include a diverse heterotypic spheroid model of two or more cell types. This would be applied to study tissue development and organization. The optimal conditions that contribute to the self-assembly of tissues mimicking their normal behavior in vivo, including vascularization, can be assessed using our chip.

The present tumor-on-a-chip benefits from scalability (**Fig. S4-6**), allowing clinicians to measure results and automate data collection and interpretation (**Fig. S7**). We also presented a modified g-code tool that allows for the automation and ease of design for those who are not able to use any 3D design tool during the bioprinting process, a step that is crucial for high-throughput applications and clinical trials. The low-cost chips are simple and can be manufactured using a benchtop system. Our scalability represents an advancement in cancer modeling. Our chip can be employed to study drug cytotoxicity, signaling pathways, and cell-drug interactions. Future steps would include adding more organotypic cellular components (e.g., stromal cells) to the chip and comparing the cell response for the commercial cell line with that of patient-derived primary cells.

Declaration of competing interest

The authors declare that they have no known competing financial interests or personal relationships that could have appeared to influence the work reported in this paper.

CRediT authorship contribution statement

Elvan Dogan: Data curation, Formal analysis, Methodology, Validation, Visualization, Writing – original draft, Writing – review & editing. **Christopher A. Galifi:** Data curation, Formal analysis, Writing – review & editing. **Berivan Cecen:** Investigation, Methodology. **Roshni Shukla:** Data curation, Methodology. **Teresa L. Wood:** Conceptualization, Supervision, Writing – review & editing. **Amir K. Miri:** Conceptualization, Funding acquisition, Methodology, Supervision, Writing – original draft, Writing – review & editing.

Acknowledgments

A.K.M. acknowledges the support of NIH-R01DC018577 and NSF-2243506 grants. T.L.W. acknowledges support of NIH-R01CA204312. E.D. and A.K.M. thank all lab members for their valuable feedback and comments on this manuscript. The authors thank Dr. Mary Alpaugh and Mr. Jason Da-Cunza (Department of Molecular and Cellular Biosciences, Rowan University) for their contributions to this project on our first trials of immunostaining protocol (not included here) and interpreting our initial results (preliminary data collection; not included here). E.D. and A.K.M. also thank Mr. Nathan Damien, Mr. Ryan Lancaster, Mr. Marc Schwalm, and Ms. Stephanie Pierce (College of Engineering, Rowan University) for their valuable contributions while preparing our MATLAB tools.

Supplementary materials

Supplementary material associated with this article can be found, in the online version, at doi:10.1016/j.actbio.2024.07.040.

References

- [1] M. Buchanan, C. Chabot, J. Lafleur, U. Krzemien, C. Lan, O. Savichtcheva, J.-F. Boileau, C. Ferrario, P. Savage, M. Park, Use of PDXs and patient-derived cell lines to uncover unconventional drug therapies and combinations for the treatment of drug-resistant cancers, AACR (2018).
- [2] L. Garcia-Martinez, Y. Zhang, Y. Nakata, H.L. Chan, L. Morey, Epigenetic mechanisms in breast cancer therapy and resistance, Nat. Commun. 12 (1) (2021) 1–14.
- [3] A.C. SocietyWhat is a Soft Tissue Sarcoma?, 2019 https://www.cancer. org/cancer/soft-tissue-sarcoma/about/soft-tissue-sarcoma.html (Accessed 29 March 2020).
- [4] M.M. Khan, S. Waqar, R.A. Mahmood, M. Zahid, Surgical management of soft tissue sarcoma, J. Rawalpindi Med. Coll. (2018) 58–62.
- [5] E. Dogan, F. Salemizadehparizi, B. Cecen, A.K. Miri, Chapter 3 Recent advances in tumors-on-chips, in: G. Gonçalves, P. Marques, J. Mano (Eds.), New Trends in Smart Nanostructured Biomaterials in Health Sciences, Elsevier 2023, pp. 79–117.
- [6] P. Zhuang, Y.H. Chiang, M.S. Fernanda, M. He, Using Spheroids as Building Blocks Towards 3D Bioprinting of Tumor Microenvironment, Int. J. Bioprint. 7 (4) (2021) 444.
- [7] S. Aparicio, M. Hidalgo, A.L. Kung, Examining the utility of patient-derived xenograft mouse models, Nat. Rev. Cancer 15 (5) (2015) 311–316.
- [8] A.T. Byrne, D.G. Alférez, F. Amant, D. Annibali, J. Arribas, A.V. Biankin, A. Bruna, E. Budinská, C. Caldas, D.K. Chang, R.B. Clarke, H. Clevers, G. Coukos, V. Dangles-Marie, S.G. Eckhardt, E. Gonzalez-Suarez, E. Hermans, M. Hidalgo, M.A. Jarzabek, S. de Jong, J. Jonkers, K. Kemper, L. Lanfrancone, G.M. Mælandsmo, E. Marangoni, J.-C. Marine, E. Medico, J.H. Norum, H.G. Palmer, D.S. Peeper, P.G. Pelicci, A. Piris-Gimenez, S. Roman-Roman, O.M. Rueda, J. Seoane, V. Serra, L. Soucek, D. Vanhecke, A. Villanueva, E. Vinolo, A. Bertotti, L. Trusolino, Interrogating open issues in cancer precision medicine with patient-derived xenografts, Nat. Rev. Cancer 17 (4) (2017) 254–268.
- [9] S.-Y. Jo, E. Kim, S. Kim, Impact of mouse contamination in genomic profiling of patient-derived models and best practice for robust analysis, Genome Biol. 20 (1) (2019) 231.
- [10] B. Patra, J. Lafontaine, M. Bavoux, K. Zerouali, A. Glory, M. Ahanj, J.-F. Carrier, T. Gervais, P. Wong, On-chip combined radiotherapy and chemotherapy testing on soft-tissue sarcoma spheroids to study cell death using flow cytometry and clonogenic assay, Sci. Rep. 9 (1) (2019) 2214.
- [11] A. Miri, E. Mostafavi, D. Khorsandi, S.-K. Hu, M. Malpica, A. Khademhosseini, Bioprinters for organs-on-chips, Biofabrication (2019).
- [12] O. Yesil-Celiktas, S. Hassan, A.K. Miri, S. Maharjan, R. Al-kharboosh, A. Quiñones-Hinojosa, Y.S. Zhang, Mimicking human pathophysiology in organ-on-chip devices, Adv. Biosyst. 0 (0) (2018) 1800109.
- [13] D.L. Hughes, A. Hughes, Z. Soonawalla, S. Mukherjee, E. O'Neill, Dynamic physiological culture of ex vivo human tissue: a systematic review, Cancers 13 (12) (2021).
- [14] X. Wan, S. Ball, F. Willenbrock, S. Yeh, N. Vlahov, D. Koennig, M. Green, G. Brown, S. Jeyaretna, Z. Li, Z. Cui, H. Ye, E. O'Neill, Perfused three-dimensional organotypic culture of human cancer cells for therapeutic evaluation, Sci. Rep. 7 (1) (2017) 9408.
- [15] E. Refet-Mollof, O. Najyb, R. Chermat, A. Glory, J. Lafontaine, P. Wong, T. Gervais, Hypoxic Jumbo Spheroids On-A-Chip (HOnAChip): insights into treatment efficacy, Cancers 13 (16) (2021) 4046.
- [16] Y. Jiang, H. Zhang, J. Wang, Y. Liu, T. Luo, H. Hua, Targeting extracellular matrix stiffness and mechanotransducers to improve cancer therapy, J. Hematol. Oncol. 15 (1) (2022) 34.
- [17] S. Ishihara, H. Haga, Matrix stiffness contributes to cancer progression by regulating transcription factors, Cancers 14 (4) (2022).

- [18] C.H. Lin, F.A. Pelissier, H. Zhang, J. Lakins, V.M. Weaver, C. Park, M.A. LaBarge, Microenvironment rigidity modulates responses to the HER2 receptor tyrosine kinase inhibitor lapatinib via YAP and TAZ transcription factors, Mol. Biol. Cell 26 (22) (2015) 3946–3953.
- [19] B. Jin, W. Kong, X. Zhao, S. Chen, Q. Sun, J. Feng, D. Song, D. Han, Substrate stiffness affects the morphology, proliferation, and radiosensitivity of cervical squamous carcinoma cells, Tissue Cell 74 (2022) 101681.
- [20] B. Deng, Z. Zhao, W. Kong, C. Han, X. Shen, C. Zhou, Biological role of matrix stiffness in tumor growth and treatment, J. Transl. Med. 20 (1) (2022) 540.
- [21] A. Malandrino, X. Trepat, R.D. Kamm, M. Mak, Dynamic filopodial forces induce accumulation, damage, and plastic remodeling of 3D extracellular matrices, PLoS Comput. Biol. 15 (4) (2019) e1006684.
- [22] Y. Liang, J. Jeong, R.J. DeVolder, C. Cha, F. Wang, Y.W. Tong, H. Kong, A cell-in-structive hydrogel to regulate malignancy of 3D tumor spheroids with matrix rigidity, Biomaterials 32 (35) (2011) 9308–9315.
 [23] A.H. Mekhdjian, F. Kai, M.G. Rubashkin, L.S. Prahl, L.M. Przybyla, A.L. McGre-
- [23] A.H. Mekhdjian, F. Kai, M.G. Rubashkin, L.S. Prahl, L.M. Przybyla, A.L. McGregor, E.S. Bell, J.M. Barnes, C.C. DuFort, G. Ou, A.C. Chang, L. Cassereau, S.J. Tan, M.W. Pickup, J.N. Lakins, X. Ye, M.W. Davidson, J. Lammerding, D.J. Odde, A.R. Dunn, V.M. Weaver, Integrin-mediated traction force enhances paxillin molecular associations and adhesion dynamics that increase the invasiveness of tumor cells into a three-dimensional extracellular matrix, Mol. Biol. Cell 28 (11) (2017) 1467-1488.
- [24] Y. Lin, K. Yuan, Y. Yang, S. Yang, K. Huang, Z. Yu, S. Zhang, Y. Liu, H. Li, Y. Dong, T. Tang, Osteosarocma progression in biomimetic matrix with different stiffness: insights from a three-dimensional printed gelatin methacrylamide hydrogel, Int. J. Biol. Macromol. 252 (2023) 126391.
- [25] V. Pankova, L. Krasny, W. Kerrison, Y.B. Tam, M. Chadha, J. Burns, C.P. Wilding, L. Chen, A. Chowdhury, E. Perkins, A.T.J. Lee, L. Howell, N. Guljar, K. Sisley, C. Fisher, P. Chudasama, K. Thway, R.L. Jones, P.H. Huang, Clinical implications and molecular features of extracellular matrix networks in soft tissue sarcomas, Clin. Cancer Res. (2024).
- [26] H.-R. Jung, H.M. Kang, J.-W. Ryu, D.-S. Kim, K.H. Noh, E.-S. Kim, H.-J. Lee, K.-S. Chung, H.-S. Cho, N.-S. Kim, D.-S. Im, J.H. Lim, C.-R. Jung, Cell spheroids with enhanced aggressiveness to mimic human liver cancer in vitro and in vivo, Sci. Rep. 7 (1) (2017) 10499.
- [27] X. Sun, X. Lv, Y. Yan, Y. Zhao, R. Ma, M. He, M. Wei, Hypoxia-mediated cancer stem cell resistance and targeted therapy, Biomed. PharmacOther 130 (2020) 110623
- [28] W. Zeng, P. Liu, W. Pan, S.R. Singh, Y. Wei, Hypoxia and hypoxia inducible factors in tumor metabolism, Cancer Lett. 356 (2 Pt A) (2015) 263–267.
- [29] D. Lachowski, E. Cortes, A. Rice, D. Pinato, K. Rombouts, A. Del Rio Hernandez, Matrix stiffness modulates the activity of MMP-9 and TIMP-1 in hepatic stellate cells to perpetuate fibrosis, Sci. Rep. 9 (1) (2019) 7299.
- [30] G. Safarians, A. Sohrabi, I. Solomon, W. Xiao, S. Bastola, B.W. Rajput, M. Epperson, I. Rosenzweig, K. Tamura, B. Singer, J. Huang, M.J. Harrison, T. Sanazzaro, M.C. Condro, H.I. Kornblum, S.K. Seidlits, Glioblastoma spheroid invasion through soft, brain-like matrices depends on hyaluronic acid-CD44 interactions, Adv. Healthc. Mater. 12 (14) (2023) e2203143.
- [31] E. Dogan, A. Kisim, G. Bati-Ayaz, G.J. Kubicek, D. Pesen-Okvur, A.K. Miri, Cancer stem cells in tumor modeling: challenges and future directions, Adv. Nanobiomed. Res. 1 (11) (2021) 2100017.
- [32] S. Swaminathan, Q. Hamid, W. Sun, A.M. Clyne, Bioprinting of 3D breast epithelial spheroids for human cancer models, Biofabrication. 11 (2) (2019) 025003
- [33] S. Lu, F. Cuzzucoli, J. Jiang, L.-G. Liang, Y. Wang, M. Kong, X. Zhao, W. Cui, J. Li, S. Wang, Development of a biomimetic liver tumor-on-a-chip model based on decellularized liver matrix for toxicity testing, Lab. Chip. 18 (22) (2018) 3379–3392
- [34] D. Wang, Y. Guo, J. Zhu, F. Liu, Y. Xue, Y. Huang, B. Zhu, D. Wu, H. Pan, T. Gong, Y. Lu, Y. Yang, Z. Wang, Hyaluronic acid methacrylate/pancreatic extracellular matrix as a potential 3D printing bioink for constructing islet organoids, Acta Biomater. 165 (2023) 86–101.
- [35] F. Davoudi, S. Ghorbanpoor, S. Yoda, X. Pan, G.S. Crowther, X. Yin, E. Murchie, A.N. Hata, H. Willers, C.H. Benes, Alginate-based 3D cancer cell culture for therapeutic response modeling, STAR. Protoc. 2 (2) (2021) 100391.
- [36] J. Duan, Y. Cao, Z. Shen, Y. Cheng, Z. Ma, L. Wang, Y. Zhang, Y. An, S. Sang, 3D bioprinted GelMA/PEGDA hybrid scaffold for establishing an in vitro model of melanoma, J. Microbiol. Biotechnol. 32 (4) (2022) 531–540.
- [37] W. Shi, S. Mirza, M. Kuss, B. Liu, A. Hartin, S. Wan, Y. Kong, B. Mohapatra, M. Krishnan, H. Band, V. Band, B. Duan, Embedded bioprinting of breast tumor cells and organoids using low-concentration collagen-based bioinks, Adv. Healthc. Mater. 12 (26) (2023) e2300905.
- [38] C. Lee, E. Abelseth, L. de la Vega, S.M. Willerth, Bioprinting a novel glioblastoma tumor model using a fibrin-based bioink for drug screening, Mater. Today Chem. 12 (2019) 78–84.
- [39] G.R. López-Marcial, A.Y. Zeng, C. Osuna, J. Dennis, J.M. García, G.D. O'Connell, Agarose-based hydrogels as suitable bioprinting materials for tissue engineering, ACS Biomater. Sci. Eng. 4 (10) (2018) 3610–3616.
- [40] S. Talukdar, M. Mandal, D.W. Hutmacher, P.J. Russell, C. Soekmadji, S.C. Kundu, Engineered silk fibroin protein 3D matrices for in vitro tumor model, Biomaterials 32 (8) (2011) 2149–2159.
- [41] I. Pepelanova, K. Kruppa, T. Scheper, A. Lavrentieva, Gelatin-Methacryloyl (GelMA) hydrogels with defined degree of functionalization as a versatile toolkit for 3D cell culture and extrusion bioprinting, Bioengineering 5 (3) (2018) 55.

- [42] F. Ruedinger, A. Lavrentieva, C. Blume, I. Pepelanova, T. Scheper, Hydrogels for 3D mammalian cell culture: a starting guide for laboratory practice, Appl. Microbiol. Biotechnol. 99 (2) (2015) 623–636.
- [43] N.S. Bhise, V. Manoharan, S. Massa, A. Tamayol, M. Ghaderi, M. Miscuglio, Q. Lang, Y. Shrike Zhang, S.R. Shin, G. Calzone, N. Annabi, T.D. Shupe, C.E. Bishop, A. Atala, M.R. Dokmeci, A. Khademhosseini, A liver-on-a-chip platform with bioprinted hepatic spheroids. Biofabrication. 8 (1) (2016) 014101.
- [44] A.I. Van Den Bulcke, B. Bogdanov, N. De Rooze, E.H. Schacht, M. Cornelissen, H. Berghmans, Structural and rheological properties of methacrylamide modified gelatin hydrogels, Biomacromolecules 1 (1) (2000) 31–38.
 [45] N. Peela, F.S. Sam, W. Christenson, D. Truong, A.W. Watson, G. Mouneimne,
- [45] N. Peela, F.S. Sam, W. Christenson, D. Truong, A.W. Watson, G. Mouneimne, R. Ros, M. Nikkhah, A three dimensional micropatterned tumor model for breast cancer cell migration studies, Biomaterials 81 (2016) 72–83.
- [46] D. Loessner, C. Meinert, E. Kaemmerer, L.C. Martine, K. Yue, P.A. Levett, T.J. Klein, F.P.W. Melchels, A. Khademhosseini, D.W. Hutmacher, Functionalization, preparation and use of cell-laden gelatin methacryloyl-based hydrogels as modular tissue culture platforms, Nat. Protoc. 11 (4) (2016) 727–746.
- [47] A.D. Arya, P.M. Hallur, A.G. Karkisaval, A. Gudipati, S. Rajendiran, V. Dhavale, B. Ramachandran, A. Jayaprakash, N. Gundiah, A. Chaubey, Gelatin methacry-late hydrogels as biomimetic three-dimensional matrixes for modeling breast cancer invasion and chemoresponse in vitro, ACS. Appl. Mater. Interfaces. 8 (34) (2016) 22005–22017.
- [48] A.K. Miri, H.G. Hosseinabadi, B. Cecen, S. Hassan, Y.S. Zhang, Permeability mapping of gelatin methacryloyl hydrogels, Acta Biomater. 77 (2018) 38-47.
- [49] Y. Piao, H. You, T. Xu, H.-P. Bei, I.Z. Piwko, Y.Y. Kwan, X. Zhao, Biomedical applications of gelatin methacryloyl hydrogels, Eng. Regener. 2 (2021) 47–56.
- [50] S. Bupphathong, C. Quiroz, W. Huang, P.F. Chung, H.Y. Tao, C.H. Lin, Gelatin methacrylate hydrogel for tissue engineering applications-a review on material modifications, Pharmaceuticals 15 (2) (2022).
- [51] A.D. Arya, P.M. Hallur, A.G. Karkisaval, A. Gudipati, S. Rajendiran, V. Dhavale, B. Ramachandran, A. Jayaprakash, N. Gundiah, A. Chaubey, Gelatin methacry-late hydrogels as biomimetic three-dimensional matrixes for modeling breast cancer invasion and chemoresponse in vitro, ACS. Appl. Mater. Interfaces 8 (34) (2016) 22005–22017.
- [52] A. Bessot, J. Gunter, D. Waugh, J.A. Clements, D.W. Hutmacher, J. McGovern, N. Bock, GelMA and biomimetic culture allow the engineering of mineralized, adipose, and tumor tissue human microenvironments for the study of advanced prostate cancer in vitro and in vivo, Adv. Healthc. Mater. 12 (14) (2023) 2201701
- [53] E. Dogan, C. Holshue, A. Bhusal, R. Shukla, A.K. Miri, Cell encapsulation in gelatin methacryloyl bioinks impairs microscale diffusion properties, Front. Bioeng. Biotechnol. 11 (2023) 1193970.
- [54] L. Neufeld, E. Yeini, N. Reisman, Y. Shtilerman, D. Ben-Shushan, S. Pozzi, A. Madi, G. Tiram, A. Eldar-Boock, S. Ferber, R. Grossman, Z. Ram, R. Satchi– Fainaro, Microengineered perfusable 3D-bioprinted glioblastoma model for in vivo mimicry of tumor microenvironment, Sci. Adv. 7 (34) (2021) eabi9119.
- [55] W. Schuurman, P.A. Levett, M.W. Pot, P.R. van Weeren, W.J. Dhert, D.W. Hutmacher, F.P. Melchels, T.J. Klein, J. Malda, Gelatin-methacrylamide hydrogels as potential biomaterials for fabrication of tissue-engineered cartilage constructs, Macromol. Biosci. 13 (5) (2013) 551–561.
- [56] S.M. Wilhelm, A.Z. Eisen, M. Teter, S.D. Clark, A. Kronberger, G. Goldberg, Human fibroblast collagenase: glycosylation and tissue-specific levels of enzyme synthesis, Proc. Natl. Acad. Sci. 83 (11) (1986) 3756–3760.
- [57] M. Zhu, Y. Wang, G. Ferracci, J. Zheng, N.-J. Cho, B.H. Lee, Gelatin methacryloyl and its hydrogels with an exceptional degree of controllability and batch-tobatch consistency, Sci. Rep. 9 (1) (2019) 6863.
- [58] P.Y. Muller, H. Janovjak, A.R. Miserez, Z. Dobbie, Processing of gene expression data generated by quantitative real-time RT-PCR, Biotechniques 32 (6) (2002) 1372–1374 1376, 1378-9.
- [59] R.L.F. Amaral, M. Miranda, P.D. Marcato, K. Swiech, Comparative analysis of 3D bladder tumor spheroids obtained by forced floating and hanging drop methods for drug screening, Front. Physiol. 8 (2017) 605.
- [60] B.M. Leung, S.C. Lesher-Perez, T. Matsuoka, C. Moraes, S. Takayama, Media additives to promote spheroid circularity and compactness in hanging drop platform, Biomater. Sci. 3 (2) (2015) 336–344.
- [61] X. Gong, C. Lin, J. Cheng, J. Su, H. Zhao, T. Liu, X. Wen, P. Zhao, Generation of multicellular tumor spheroids with microwell-based agarose scaffolds for drug testing, PLoS ONE 10 (6) (2015) e0130348.
- [62] A.R. Donaldson, C.E. Tanase, D. Awuah, P. Vasanthi Bathrinarayanan, L. Hall, M. Nikkhah, A. Khademhosseini, F. Rose, C. Alexander, A.M. Ghaemmaghami, Photocrosslinkable gelatin hydrogels modulate the production of the major pro-inflammatory cytokine, TNF-α, by human mononuclear cells, Front. Bioeng, Biotechnol. 6 (116) (2018).
- [63] D. Loessner, C. Meinert, E. Kaemmerer, L.C. Martine, K. Yue, P.A. Levett, T.J. Klein, F.P. Melchels, A. Khademhosseini, D.W. Hutmacher, Functionalization, preparation and use of cell-laden gelatin methacryloyl-based hydrogels as modular tissue culture platforms, Nat. Protoc. 11 (4) (2016) 727–746.
- [64] J.W. Nichol, S.T. Koshy, H. Bae, C.M. Hwang, S. Yamanlar, A. Khademhosseini, Cell-laden microengineered gelatin methacrylate hydrogels, Biomaterials 31 (21) (2010) 5536–5544.
- [65] K. Pepin, R. Grimm, S. Kargar, B.M. Howe, K. Fritchie, M. Frick, D. Wenger, S. Okuno, R. Ehman, K. McGee, S. James, N. Laack, M. Herman, D. Pafundi, Soft tissue sarcoma stiffness and perfusion evaluation by MRE and DCE-MRI for radiation therapy response assessment: a technical feasibility study, Biomed. Phys. Eng. Express. 5 (4) (2019), doi:10.1088/2057-1976/ab2175.

- [66] A. Bhusal, E. Dogan, H.A. Nguyen, O. Labutina, D. Nieto, A. Khademhosseini, A.K. Miri, Multi-material digital light processing bioprinting of hydrogel-based microfluidic chips, Biofabrication. 14 (1) (2021).
- [67] Y.M. Efremov, I.M. Zurina, V.S. Presniakova, N.V. Kosheleva, D.V. Butnaru, A.A. Svistunov, Y.A. Rochev, P.S. Timashev, Mechanical properties of cell sheets and spheroids: the link between single cells and complex tissues, Biophys. Rev. 13 (4) (2021) 541–561.
- [68] Q. Xiao, G. Ge, Lysyl oxidase, extracellular matrix remodeling and cancer metastasis, Cancer Microenviron. 5 (3) (2012) 261–273.
- [69] M. Ehrbar, A. Sala, P. Lienemann, A. Ranga, K. Mosiewicz, A. Bittermann, S.C. Rizzi, F.E. Weber, M.P. Lutolf, Elucidating the role of matrix stiffness in 3D cell migration and remodeling, Biophys. J. 100 (2) (2011) 284–293.
- [70] A.A. Solbu, D. Caballero, S. Damigos, S.C. Kundu, R.L. Reis, Ø. Halaas, A.S. Chahal, B.L. Strand, Assessing cell migration in hydrogels: an overview of relevant materials and methods. Mater. Today Bio 18 (2023) 100537.
- [71] X. Di, X. Gao, L. Peng, J. Ai, X. Jin, S. Qi, H. Li, K. Wang, D. Luo, Cellular mechanotransduction in health and diseases: from molecular mechanism to therapeutic targets, Signal. Transduct. Target. Ther. 8 (1) (2023) 282.
- [72] J.A. McGlynn, K.M. Schultz, Measuring human mesenchymal stem cell remodeling in hydrogels with a step-change in elastic modulus, Soft. Matter. 18 (34) (2022) 6340–6352.
- [73] L. Figueiredo, R. Pace, C. D'Arros, G. Réthoré, J. Guicheux, C.Le Visage, P. Weiss, Assessing glucose and oxygen diffusion in hydrogels for the rational design of 3D stem cell scaffolds in regenerative medicine, J. Tissue Eng. Regen. Med. 12 (5) (2018) 1238–1246.
- [74] S. Riffle, R.S. Hegde, Modeling tumor cell adaptations to hypoxia in multicellular tumor spheroids, J. Exp. Clin. Cancer Res. 36 (1) (2017) 102.
- [75] D.-H. Kim, S.B. Khatau, Y. Feng, S. Walcott, S.X. Sun, G.D. Longmore, D. Wirtz, Actin cap associated focal adhesions and their distinct role in cellular mechanosensing, Sci. Rep. 2 (1) (2012) 555.
- [76] D.-H. Kim, A.B. Chambliss, D. Wirtz, The multi-faceted role of the actin cap in cellular mechanosensation and mechanotransduction, Soft. Matter. 9 (23) (2013) 5516–5523.
- [77] C.R. Lam, H.K. Wong, S. Nai, C.K. Chua, N.S. Tan, L.P. Tan, A 3D biomimetic model of tissue stiffness interface for cancer drug testing, Mol. Pharm. 11 (7) (2014) 2016–2021.
- [78] A. Zieseniss, Hypoxia and the modulation of the actin cytoskeleton emerging interrelations, Hypoxia 2 (2014) 11–21.
- [79] M. Vicente-Manzanares, C.K. Choi, A.R. Horwitz, Integrins in cell migration-the actin connection, J. Cell Sci. 122 (Pt 2) (2009) 199–206.
- [80] A.J. Ridley, M.A. Schwartz, K. Burridge, R.A. Firtel, M.H. Ginsberg, G. Borisy, J.T. Parsons, A.R. Horwitz, Cell migration: integrating signals from front to back, Science (1979) 302 (5651) (2003) 1704–1709.
- [81] S. Freitas-Rodríguez, A.R. Folgueras, C. López-Otín, The role of matrix metal-loproteinases in aging: tissue remodeling and beyond, Biochim. Biophys. Acta 1864 (11, Part A) (2017) 2015–2025.

- [82] P. Cancemi, A. Aiello, G. Accardi, R. Caldarella, G. Candore, C. Caruso, M. Ciaccio, L. Cristaldi, F. Di Gaudio, V. Siino, S. Vasto, The role of matrix metallo-proteinases (MMP-2 and MMP-9) in ageing and longevity: focus on sicilian long-living individuals (LLIs), Mediators Inflamm. 2020 (2020) 8635158.
- [83] K. Nabeshima, T. Inoue, Y. Shimao, T. Sameshima, Matrix metalloproteinases in tumor invasion: role for cell migration, Pathol. Int. 52 (4) (2002) 255–264.
- [84] M.S. Benassi, G. Gamberi, G. Magagnoli, L. Molendini, P. Ragazzini, M. Merli, F. Chiesa, A. Balladelli, M. Manfrini, F. Bertoni, M. Mercuri, P. Picci, Metalloproteinase expression and prognosis in soft tissue sarcomas, Ann. Oncol. 12 (1) (2001) 75–80.
- [85] H.K. Yang, K.C. Jeong, Y.K. Kim, S.T. Jung, Role of matrix metalloproteinase (MMP) 2 and MMP-9 in soft tissue sarcoma, Clin. Orthop. Surg. 6 (4) (2014) 443-454
- [86] B. Wang, Y.M. Ding, P. Fan, B. Wang, J.H. Xu, W.X. Wang, Expression and significance of MMP2 and HIF- 1α in hepatocellular carcinoma, Oncol. Lett. 8 (2) (2014) 539–546.
- [87] A. Pasini, J. Lovecchio, M. Cortesi, C. Liverani, C. Spadazzi, L. Mercatali, T. Ibrahim, E. Giordano, Perfusion flow enhances viability and migratory phenotype in 3D-cultured breast cancer cells, Ann. Biomed. Eng. 49 (9) (2021) 2103–2113
- [88] M.G. Rubashkin, L. Cassereau, R. Bainer, C.C. DuFort, Y. Yui, G. Ou, M.J. Paszek, M.W. Davidson, Y.-Y. Chen, V.M. Weaver, Force engages vinculin and promotes tumor progression by enhancing PI3K activation of phosphatidylinositol (3,4,5)-triphosphate, Cancer Res. 74 (17) (2014) 4597–4611.
- [89] B. Krishnamachary, S. Berg-Dixon, B. Kelly, F. Agani, D. Feldser, G. Ferreira, N. Iyer, J. LaRusch, B. Pak, P. Taghavi, G.L. Semenza, Regulation of colon carcinoma cell invasion by hypoxia-inducible factor 1, Cancer Res. 63 (5) (2003) 1138–1143.
- [90] S. Keleg, H. Kayed, X. Jiang, R. Penzel, T. Giese, M.W. Buchler, H. Friess, J. Kleeff, Adrenomedullin is induced by hypoxia and enhances pancreatic cancer cell invasion, Int. J. Cancer 121 (1) (2007) 21–32.
- [91] V. Bizzarro, R. Belvedere, V. Migliaro, E. Romano, L. Parente, A. Petrella, Hy-poxia regulates ANXA1 expression to support prostate cancer cell invasion and aggressiveness, Cell Adh. Migr. 11 (3) (2017) 247–260.
- [92] I. Yana, M. Seiki, MT-MMPs play pivotal roles in cancer dissemination, Clin. Exp. Metastasis 19 (3) (2002) 209–215.
- [93] M. Monteiro, V. Gaspar, L.P. Ferreira, J.F. Mano, Hydrogel 3D in vitro tumor models for screening cell aggregation mediated drug response, Biomater. Sci. 8 (2020)
- [94] R. Edmondson, J.J. Broglie, A.F. Adcock, L. Yang, Three-dimensional cell culture systems and their applications in drug discovery and cell-based biosensors, Assay. Drug Dev. Technol. 12 (4) (2014) 207–218.